Journal of Electrochemistry

Volume 30
Issue 10 *Special Issue on Single-Entity Electroanalysis*

2024-10-28

Single Nanobubble Formation on Au Nanoelectrodes and Au@WS_2 Nanoelectrodes: Voltammetric Analysis and Electrocatalysis

Xian-Zhun Luo
Anhui Province Key laboratory of biomedical materials and chemical measurement, Key Laboratory of Functional Molecular Solids, Ministry of Education, College of Chemistry and Materials Science, Anhui Normal University, Wuhu, 241000, P.R. China, 3107383795@qq.com

Xiao-Hu Chen

Yong-Xin Li
Anhui Province Key laboratory of biomedical materials and chemical measurement, Key Laboratory of Functional Molecular Solids, Ministry of Education, College of Chemistry and Materials Science, Anhui Normal University, Wuhu, 241000, P.R. China, yongli@mail.ahnu.edu.cn

Recommended Citation

Xian-Zhun Luo, Xiao-Hu Chen, Yong-Xin Li. Single Nanobubble Formation on Au Nanoelectrodes and Au@WS_2 Nanoelectrodes: Voltammetric Analysis and Electrocatalysis[J]. *Journal of Electrochemistry*, 2024 , 30(10): 2414001.
DOI: 10.61558/2993-074X.3475
Available at: https://jelectrochem.xmu.edu.cn/journal/vol30/iss10/1

ARTICLE

Single-Entity Electroanalysis

Single Nanobubble Formation on Au Nanoelectrodes and Au@WS_2 Nanoelectrodes: Voltammetric Analysis and Electrocatalysis

Xian-Zhun Luo, Xiao-Hu Chen, Yong-Xin Li*

Anhui Province Key Laboratory of Biomedical Materials and Chemical Measurement, Key Laboratory of Functional Molecular Solids, Ministry of Education, College of Chemistry and Materials Science, Anhui Normal University, Wuhu, 241000, PR China

Abstract

Taking advantage of the extremely small size of the gold nanodisk electrode, the single hydrogen nanobubble generated on the surface of the nanoelectrode was studied to evaluate its hydrogen evolution performance. It was found that compared with the bare gold nanodisk electrode, the bubble formation potential of the gold nanodisk electrode modified with tungsten disulfide quantum dots (WS_2 QDs) on the surface was more positive, indicating that its hydrogen evolution activity was higher. Microdynamic model analysis shows that the average standard rate constant of the rate-determining step of the hydrogen evolution reaction of gold nanoelectrodes modified with WS_2 QDs is approximately 12 times larger than that of gold nanoelectrodes. This work based on the formation of nanobubbles provides new ideas for the design and performance evaluation of hydrogen evolution reaction catalysts.

Keywords: Nanoelectrode; Nanobubble; Electrocatalysis

1. Introduction

Today, solar energy, hydrogen energy, nuclear energy, etc. have attracted much attention, and the most important issue in the current development process of new energy sources is how to effectively realize the conversion, storage and utilization of these renewable energy sources. The production of clean energy hydrogen by electrolyzing water consists of hydrogen evolution reaction (HER) and oxygen evolution reaction (OER) [1−4]. In the fuel cell, the hydrazine hydrate at the anode is oxidized to generate nitrogen [5,6]. In the chlor-alkali industry, an anodic oxidation produces chlorine, methanol oxidation reaction, etc. This series of gas evolution reactions form the basis of the electrochemical industry. Due to the extensive research and application of nanoparticles, clusters and even single atoms as catalysts for gas evolution chemical processes, the study of gas nanobubbles on the surface of nanocatalysts, especially their formation, growth and detachment, has attracted more and more scientific researchers [7−11]. The electrochemistry of nanobubbles has only begun to receive attention in recent years, and nanoelectrodes have been developed as unique tools that enable the quantitative study of individual gas nanobubbles [12−18].

In this work, we explored the nucleation of single hydrogen nanobubbles on gold nanoelectrodes (Au NEs, radius <50 nm), and evaluated the hydrogen evolution reaction (HER) activities of gold nanoelectrodes (Au NEs) and gold@tungsten disulfide quantum dot nanoelectrodes (Au@WS_2 NEs) through microdynamic models. The results showed that the critically dissolved hydrogen concentration on the surface of Au NEs is approximately 0.4 $mol \cdot L^{-1}$. In addition, through the microdynamic analysis before the formation of a single nanobubble,

Received 9 April 2024; Received in revised form 19 May 2024; Accepted 22 May 2024
Available online 30 May 2024

* Corresponding author, Yong-Xin Li, E-mail address: yongli@mail.ahnu.edu.cn.

https://doi.org/10.61558/2993-074X.3475

it was found that the rate-determining steps of HER from the Au@WS_2 NEs and Au NEs are Heyrovsky step and Volmer step, respectively, and the standard rate constant (k^0) of the rate-determining step of Au@WS_2 NEs is about 12 times that of Au NEs. This work demonstrates a basic research on nanobubble electrochemistry and provides new ideas for subsequent bubble-based applications.

2. Experimental section

2.1. Chemicals and materials

Sodium tungstate dihydrate ($Na_2WO_4 \cdot 2H_2O$, >98%) and reduced glutathione (GSH, >98%) required for the synthesis of WS_2 QDs were provided by Shanghai Titan Scientific Co., Ltd. The ferrocene (Fc, 98%), acetonitrile (ACN, AR, >98%, GC), and sulfuric acid (H_2SO_4, AR, 95%−98%) required in the experiment were purchased from Sinopharm Chemical Reagent Co., Ltd. Aluminosilicate glasses (O.D.: 1.0 mm, I.D.: 0.64 mm, length: 10 cm) were purchased from Shutter Instrument Co., Ltd. (Novato, U.S.A.).

2.2. Instrumentation and measurements

The Au nanoelectrodes (Au NEs) were prepared from a laser-assisted puller (P-2000 mode, Sutter Instrument Co., USA), and the continuity of nanotips was checked by a biological optical microscope (BX53 + DP72, Olympus, Japan). The morphologies of WS2 QDs were examined by a transmission electron microscope (TEM, HT7700 mode, Hitachi, Japan). The mapping and energy dispersive spectroscopic (EDS) analyses of the Au NEs and Au@WS_2 NEs were done by Regulus8100 microscope (Hitachi, Japan). An CHI660D model electrochemical workstation (Chenhua Instruments, Shanghai, China) was used to perform electrochemical test, which was equipped with a three-electrode system (Au NE as the working electrode, Pt wire and saturated Ag/AgCl as the counter electrode and the reference electrode, respectively).

2.3. Fabrication of Au NEs

The Au NEs were fabricated according to our previous method [19,20]. Put the gold wire into glass capillary and drew it using the P-2000 laser-assisted puller according to the following parameters:
Program 1: Heat = 365, Filament = 4, Velocity = 25, Delay = 225, Pull = 118
Program 2: Heat = 390, Filament = 1, Velocity = 30, Delay = 120, Pull = 120
Two electrodes were obtained with extremely fine tips, and the tips were examined under a light microscope to ensure that the gold wire was continuous and not broken. The electrode was encapsulated to obtain a nanodisk electrode, and the electrode was polished with sandpaper of different mesh sizes (400−1200 mesh) until the gold wire was exposed.

2.4. Synthesis of WS_2 QDs

The WS_2 QDs were synthesized by referring to the method reported by Duan et al. [21,22] An amount of 0.0625 g $Na_2WO_4 \cdot 2H_2O$ was dissolved in 12.5 mL ultrapure water, and the pH of the solution was adjusted to 6.0 with 0.1 $mol \cdot L^{-1}$ HCl. Then, 0.8625 g GSH and 50 mL ultrapure water were added to the above solution, and followed by ultrasonic dissolution. After complete dissolution, the above reactants were transferred to a 100 mL polytetrafluoroethylene autoclave, heated at 200 °C for 9 h, and then centrifuged after natural cooling. The supernatant was WS_2 QDs. The obtained WS_2 QDs were stored at 4 °C for subsequent use.

2.5. Fabrication of Au@WS_2 NEs

In order to obtain WS_2 QDs-modified Au NEs, the pre-prepared Au NEs were inserted into the WS_2 QDs aqueous solution and incubated in an atmosphere of N_2 flow for 1 h. The WS_2 QDs could be self-assembled onto the Au NEs surface through Au−S covalent bonds [23], thereby obtaining the Au@WS_2 QDs NEs.

3. Results and discussion

3.1. Characterization of Au NEs

We drew the nanoelectrodes, encapsulated and polished them according to the method previously reported by our group, and fabricated single Au NEs with different radii [19,20]. Fig. 1A shows the cyclic voltammetric behavior of gold nanoelectrodes with different radii in 5 $mmol \cdot L^{-1}$ Fc-ACN solution (containing 0.1 $mol \cdot L^{-1}$ $TBAPF_6$). It can be clearly observed that all cyclic voltammetric curves always maintain a good steady-state "S" curve and the charging current is small, showing that single Au NEs with different radii are prepared successfully [24]. Based on the steady-state limiting current, the radius of the electrode can be calculated from Eq. 1 [25].

$$i_d = 4nFDC_b a \quad (1)$$

Where i_d is the steady-state limiting current of the nanoelectrode, n is the number of electron transfer, F is the Faraday constant, D and C_b are the diffusion coefficient (2.4×10^{-9} $m^2 \cdot s^{-1}$) and

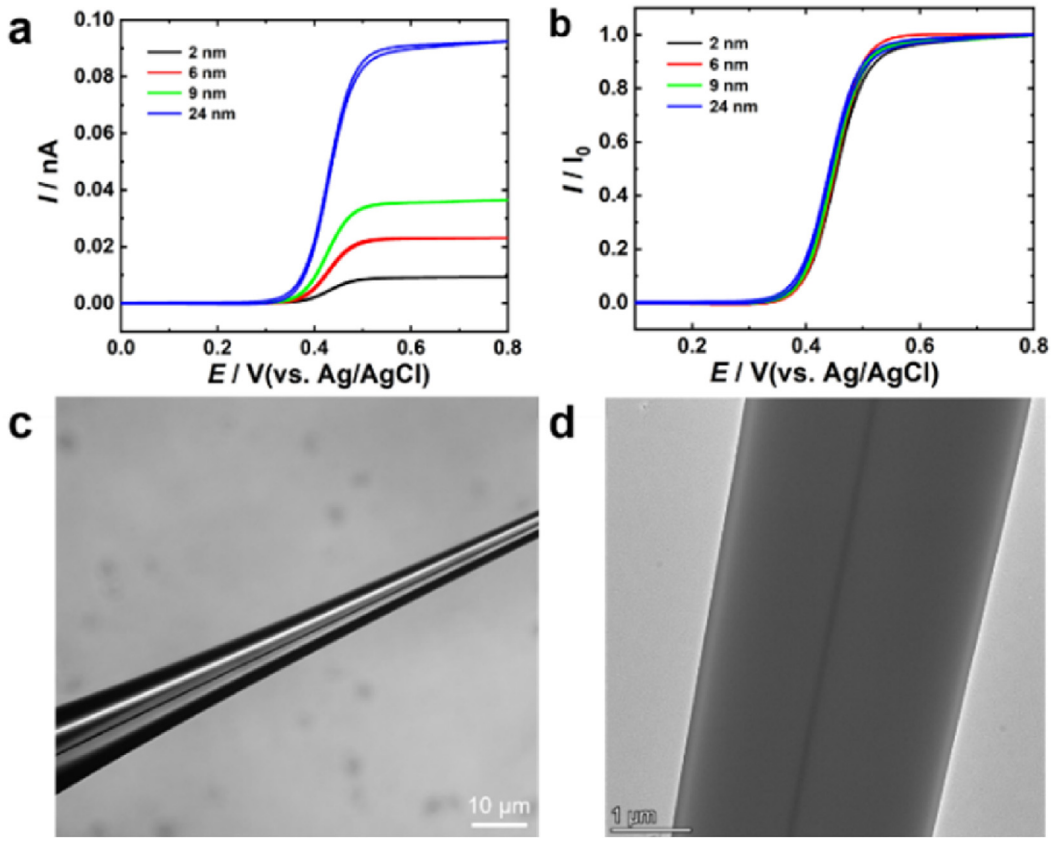

Fig. 1. (a) Voltammetric responses of single Au NEs with different sizes in a 5 mmol·L^{-1} Fc-ACN solution containing 0.1 mol·L^{-1} $TBAPF_6$. (b) Normalized current to the limiting value of the voltammetric responses of Au NEs in 5 mmol·L^{-1} Fc-ACN solution containing 0.1 mol·L^{-1} $TBAPF_6$. (c) Optical micrograph of the Au NE. (d) HRTEM image of the Au NE.

concentration of Fc-ACN, respectively, and a is the radius of the nanodisk electrode. According to the above equation, the radius values of the Au nanoelectrodes determined from the voltammetric curves shown in Fig. 1a are 2 nm (black curve), 6 nm (red curve), 9 nm (green curve), and 24 nm (blue curve). When the voltammetric current in Fig. 1a is normalized by dividing it by the corresponding limit diffusion current, the result is shown in Fig. 1b. It can be observed that with the decrease of Au NE radius, the voltammetric half-wave potential $E_{1/2}$ gradually shifts to the positive potential, indicating that the shorter the nanoelectrode radius, the faster the mass transport rate can be obtained, which is in good agreement with the results of Pt NE [25,26]. The prepared Au nanoelectrode was placed under an OLYMPUS bio-optical microscope to observe the integrity of the continuous and uniform state of the gold wire. The optical microscope image of the middle part is shown in Fig. 1c. It can be clearly seen from the image that the gold wire and the outer glass can be perfectly integrated, extending all the way to the middle, becoming even and thin, and the tip is complete and continuous without any fusion. Further through HRTEM (Fig. 1d), it can be observed that a single gold nanowire is sealed inside the glass tube with no obvious gap and a diameter of approximately 40 nm.

In addition, SEM characterization was also performed on the nanoelectrode surface. Fig. S1a is the surface of the polished Au NE, and Fig. S1b is the enlarged view of Au NE surface, where a flat, disc-shaped geometric surface can be observed, and the radius is about 25 nm. According to the results of EDS element mapping characterization (Fig. S1c, S1d), Au NEs were successfully prepared.

3.2. Characterization of WS_2 QDs

We characterized the morphology and size of the synthesized WS_2 QDs by TEM. Results from Fig. S2a show that the synthesized WS_2 QDs are spherical and well dispersed. Particle size statistics were performed on the WS_2 QDs in Fig. S2a, and the results are shown in Fig. S2b. Size distribution analysis shows that the average particle size of WS_2 QDs is 3.62 nm. We further performed EDS elemental analysis on WS_2 QDs, and the results are shown in Fig. S2c. The analysis results show that the quantum dots contain a large amount of W and S elements, the W/S atomic ratio is nearly

1:2, which agrees with the element composition of WS_2 [27,28]. The EDS spectrum also proves the successful synthesis of WS_2 QDs. Fig. S2d provides the Raman spectrum of WS_2 QDs. The characteristic peaks of E_{2g} and A_{1g} of WS_2 QDs located at 350.89 and 421.8 cm^{-1}, respectively, can be observed, which are assigned to the in-plane motion of the W/S atoms and the out-of-plane vibrations of the S atoms, respectively [27,29]. Fig. S3 shows the XPS spectra of WS_2 QDs, which was used to confirm the chemical state and elemental composition of the quantum dots. As shown in Fig. S3a, except for W and S elements, other elements show their original chemical states. The appearance of C and O is attributed to the oxidation of W element and the adsorption of CO_2 in the air on the quantum dot surface [27,30]. The bands at 32.28 and 34.48 eV (about 2.2 eV) are assigned to W $4f_{7/2}$ and W $4f_{5/2}$, respectively, and the W $5p_{3/2}$ peak can be seen at 37.88 eV (Fig. S3b), indicating that the W element of WS_2 QDs mainly exists in the +4 valence form, and the existence of W^{6+} may be due to the oxidation of the W edge during ultrasonic exfoliation and hydrothermal processes [31,32]. The bands of 161.98 and 163.08 eV belong to S $2p_{3/2}$ and S $2p_{1/2}$, respectively (Fig. S3c), which is caused by the −2 valence state of the S atom [33]. The results shown above are in good agreement with literature reported previously for 2H-WS_2 and demonstrate the successful synthesis of WS_2 QDs [33,34]. The XRD pattern of WS_2 QDs is provided in Fig. S4. For WS_2 QDs, there are only three very weak characteristic peaks correspongding to (004), (006), and (008), which is similar to the single-layer TMD quantum dots reported previously [27], revealing that the WS_2 quantum dots synthesized have the nanostructure of quantum dots.

3.3. Formation of single nanobubbles on Au NEs

Fig. 2a shows a typical cyclic voltammogram (CV) recorded on an Au NEs with a radius of 18 nm in H_2SO_4 solution. When the scan voltage is more negative than −0.5 V, the current increases rapidly, corresponding to the thermodynamic potential of proton reduction ($E(H^+/H_2)_0$), until it reaches a peak value (i_{nb}^p is about 20.23 nA), at which the voltage is approximately −0.82 V relative to Ag/AgCl. Within the range of 0 ~ −0.5 V, the *i-V* curve

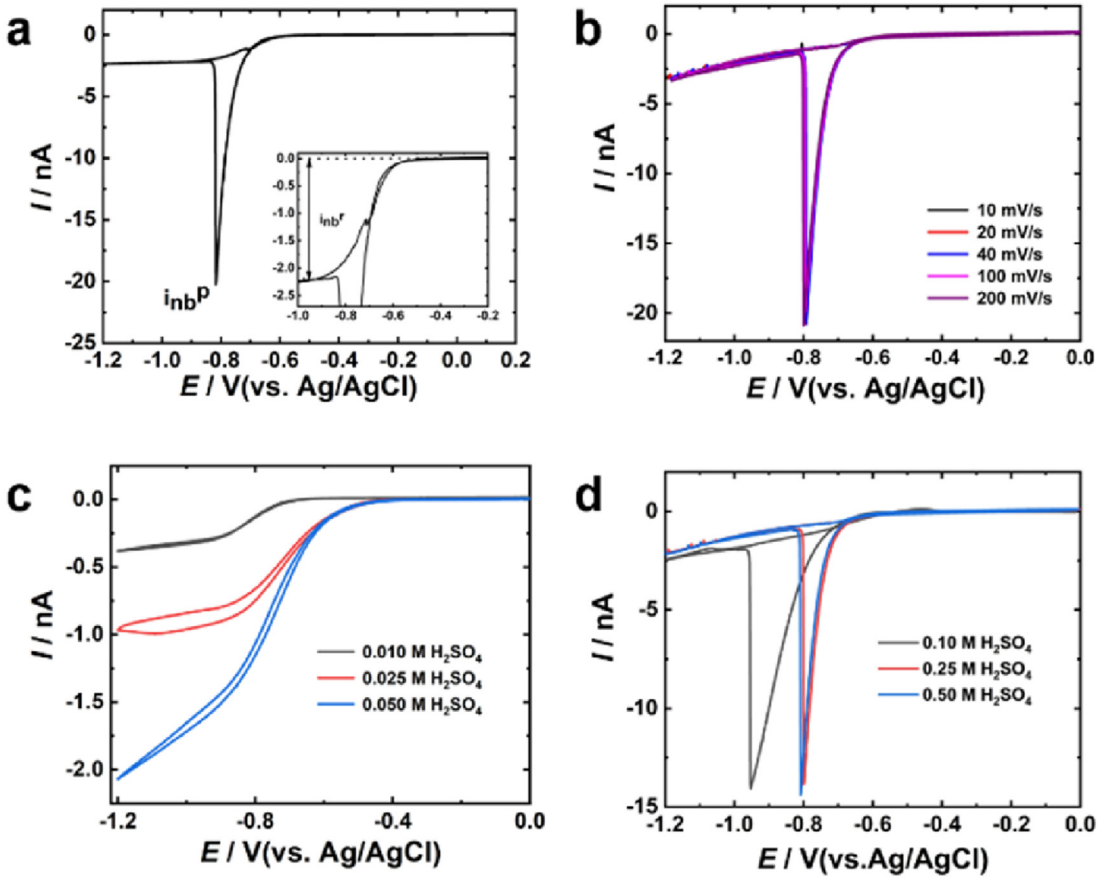

Fig. 2. (a) Cyclic voltammogram for the Au NE (20 nm radius) immersed in a N_2-purged 0.5 mol·L^{-1} H_2SO_4 solution at a scan rate of 10 mV·s^{-1}. (b) Cyclic voltammograms of the same electrode recorded at different scan rates ranging from 10 to 200 mV·s^{-1}. (c, d) Cyclic voltammetric responses of Au NE (15 nm radius) as a function of H_2SO_4 solution concentration.

is smooth and continuous, meaning that no bubble was formed. After the peak current at ~ −0.82 V, the current decreases sharply to a residual current value i_{nb}^{r} of ~ −2.2 nA. According to previous results, this voltammetric response was due to the formation of a single nanobubble on Au NE, which blocks large area of the active surface of Au NE (>95%) [12,35]. The inset in Fig. 2a shows a magnified view of the residual current after nanobubble formation. The H reduction i_{nb}^{r} remains basically unchanged, indicating that the nanobubbles at NE are in a dynamic steady state [12]. In the reverse voltammetric scan from −1.0 V to positive potential, no anodic peak H_2 nanobubbles, corresponding to the oxidation at the positive potential $E(H^+/H_2)_0$, was observed, indicating that H_2 bubbles dissolve rapidly on the voltammetric time scale once H can no longer be reduced. Fig. 2b shows the CV responses of Au NEs at different scan rates in the range of 10−200 $mV \cdot s^{-1}$, which is independent of the scan rate. Before nanobubble formation, the current is limited by H^+ transport and reduction kinetics at NE [12]. When the current reaches a critical value of ~ −21 nA, the current decreases rapidly, and nanobubbles are formed very quickly and are not affected by the scanning speed.

We also studied the electrochemical behaviors of Au NEs in different concentrations of H_2SO_4, and we can see that the shape of the CV curve gradually changes from "S-type" to "peak-type" as the concentration of H_2SO_4 increases (Fig. 2c, d). According to the mechanism of proton electroreduction to form nanobubbles on Pt NEs proposed by White et al. [12], reaching critical H_2 supersaturation on the NEs surface is important for the generation of single nanobubbles, which is related to the value of i_{nb}^{p}. When the concentration of H_2SO_4 is in the range of 0.01 $mol \cdot L^{-1}$ to 0.05 $mol \cdot L^{-1}$, it cannot reach critical H_2 supersaturation, and the maximum current is limited by the proton diffusion flux. Therefore, an S-shaped curve without nanobubble formation was obtained in Fig. 2c. However, when the concentration is larger than 0.1 $mol \cdot L^{-1}$, a peak-shaped curve with concentration-independent i_{nb}^{p} can be observed in Fig. 2d, indicating that H_2 reaches critical supersaturation on the electrode surface and single nanobubbles are generated.

3.4. Characterization of WS_2 QDs

We characterized the morphology and size of the synthesized WS_2 QDs by TEM. Results from Fig. S2a show that the synthesized WS_2 QDs are spherical and well dispersed. Particle size statistics were performed on the WS_2 QDs in Fig. S2a, and the results are shown in Fig. S2b. Size distribution analysis shows that the average particle size of WS_2 QDs is 3.62 nm. We further performed EDS elemental analysis on WS_2 QDs, and the results are shown in Fig. S2c. The analysis results show that the quantum dots contain a large amount of W and S elements, the W/S atomic ratio is nearly 1:2, which agrees with the element composition of WS_2 [27,28]. The EDS spectrum also proves the successful synthesis of WS_2 QDs. Fig. S2d provides the Raman spectrum of WS_2 QDs. The characteristic peaks of E_{2g} and A_{1g} of WS_2 QDs located at 350.89 and 421.8 cm^{-1}, respectively, can be observed, which are assigned to the in-plane motion of the W/S atoms and the out-of-plane vibrations of the S atoms, respectively [27,29].

Fig. S3 shows the XPS spectra of WS_2 QDs, which was used to confirm the chemical state and elemental composition of the quantum dots. As shown in Fig. S3a, except for W and S elements, other elements show their original chemical states. The appearance of C and O is attributed to the oxidation of W element and the adsorption of CO_2 in the air on the quantum dot surface [27,30]. The bands at 32.28 and 34.48 eV (about 2.2 eV) are assigned to W $4f_{7/2}$ and W $4f_{5/2}$, respectively, and the W $5p_{3/2}$ peak can be seen at 37.88 eV (Fig. S3b), indicating that the W element of WS_2 QDs mainly exists in the +4 valence form, and the existence of W^{6+} may be due to the oxidation of the W edge during ultrasonic exfoliation and hydrothermal processes [31,32]. The bands of 161.98 and 163.08 eV belong to S $2p_{3/2}$ and S $2p_{1/2}$, respectively (Fig. S3c), which is caused by the −2 valence state of the S atom [33]. The results shown above are in good agreement with literature reported previously for 2H-WS_2 and demonstrate the successful synthesis of WS_2 QDs [33,34]. The XRD pattern of WS_2 QDs is provided in Fig. S4. For WS_2 QDs, there are only three very weak characteristic peaks correspongding to (004), (006), and (008), which is similar to the single-layer TMD quantum dots reported previously [27], revealing that the WS_2 quantum dots synthesized have the nanostructure of quantum dots.

3.5. Formation of single nanobubbles on Au NEs

Fig. 2a shows a typical cyclic voltammogram (CV) recorded on an Au NEs with a radius of 18 nm in H_2SO_4 solution. When the scan voltage is more negative than −0.5 V, the current increases rapidly, corresponding to the thermodynamic potential of proton reduction ($E(H^+/H_2)_0$), until it reaches a peak value (i_{nb}^{p} is about 20.23 nA), at which the voltage is approximately −0.82 V relative to Ag/AgCl. Within the range of 0 ~ −0.5 V, the *i-V* curve is smooth and continuous, meaning that no bubble

was formed. After the peak current at ~ −0.82 V, the current decreases sharply to a residual current value i_{nb}^{r} of ~−2.2 nA. According to previous results, this voltammetric response was due to the formation of a single nanobubble on Au NE, which blocks large area of the active surface of Au NE (>95%) [12,35]. The inset in Fig. 2a shows a magnified view of the residual current after nanobubble formation. The H reduction i_{nb}^{r} remains basically unchanged, indicating that the nanobubbles at NE are in a dynamic steady state [12]. In the reverse voltammetric scan from −1.0 V to positive potential, no anodic peak H_2 nanobubbles, corresponding to the oxidation at the positive potential $E(H^+/H_2)_0$, was observed, indicating that H_2 bubbles dissolve rapidly on the voltammetric time scale once H can no longer be reduced. Fig. 2b shows the CV responses of Au NEs at different scan rates in the range of 10−200 $mV \cdot s^{-1}$, which is independent of the scan rate. Before nanobubble formation, the current is limited by H^+ transport and reduction kinetics at NE [12]. When the current reaches a critical value of ~ −21 nA, the current decreases rapidly, and nanobubbles are formed very quickly and are not affected by the scanning speed.

We also studied the electrochemical behaviors of Au NEs in different concentrations of H_2SO_4, and we can see that the shape of the CV curve gradually changes from "S-type" to "peak-type" as the concentration of H_2SO_4 increases (Fig. 2c, d). According to the mechanism of proton electroreduction to form nanobubbles on Pt NEs proposed by White et al. [12], reaching critical H_2 supersaturation on the NEs surface is important for the generation of single nanobubbles, which is related to the value of i_{nb}^{p}. When the concentration of H_2SO_4 is in the range of 0.01 $mol \cdot L^{-1}$ to 0.05 $mol \cdot L^{-1}$, it cannot reach critical H_2 supersaturation, and the maximum current is limited by the proton diffusion flux. Therefore, an S-shaped curve without nanobubble formation was obtained in Fig. 2c. However, when the concentration is larger than 0.1 $mol \cdot L^{-1}$, a peak-shaped curve with concentration-independent i_{nb}^{p} can be observed in Fig. 2d, indicating that H_2 reaches critical supersaturation on the electrode surface and single nanobubbles are generated.

We compared the cyclic voltammetric curves of Au NEs obtained with different radii in H_2SO_4 solution (0.5 $mol \cdot L^{-1}$). For the NEs with r < 60 nm, a "peak-type" cyclic voltammetric response can be obtained (Fig. S5a, S5b, S5c), while for the NEs with r > 60 nm, an "S-type" cyclic voltammetric response can be obtained, but there is obvious hysteresis in forward and reverse scans (Fig. S5d). The value of i_{nb}^{p} increases as the radius of NEs increases. However, for Au NEs with a radius larger than 60 nm, the maximum current approaches the diffusion-limited current. Taking the Au NE with a radius of 143 nm as an example, the maximum current observed from Fig. S5d is about −283 nA, which is close to the calculated ~−295 nA according to Eq. 1. The appearance of "S-type" on larger-sized electrodes may be caused by insufficient nanobubbles generated covering the entire electrode surface [12].

3.6. Bubble nucleation conditions of Au NEs

According to the cyclic voltammogram, changes in voltammetric current are produced by proton reduction. Before bubble nucleation, the system is in a steady-state, and the steady-state dissolved H_2 concentration (C_{H_2}) on the electrode surface can be estimated from the peak current by Eq. 2 [12,35].

$$i_{nb}^{p} = 4nFD_{H_2}C_{H_2,critical}^{s}a \quad (2)$$

where n is the number of electrons transferred per molecule of H_2 generated ($n = 2$), F is Faraday's constant (96,485C $\cdot mol^{-1}$), D_{H_2} is the diffusion coefficient of H_2 (4.5×10^{-5} $cm^2 \cdot s^{-1}$), and $C_{H_2,critical}^{s}$ is the concentration of H_2 on the NE surface. It can be seen from Eq. 2 that i_{nb}^{p} is related to the radius of the electrode (a) and the $C_{H_2,critical}^{s}$. According to our measurements of Au NEs with different radii in H_2SO_4, i_{nb}^{p} is proportional to the radius of nanoelectrode (Fig. 3a). The slope (i_{nb}^{p}/a) that can be derived from the linear relationship between i_{nb}^{p} and a is ~0.12. And according to Eq. 2, $C_{H_2,critical}^{s}$ is calculated to be approximately 0.4 $mol \cdot L^{-1}$, which is similar to the results reported in the literature [36]. Fig. 3b shows that the $C_{H_2,critical}^{s}$ for the formation of H_2 nanobubbles on the surface of NEs is relatively constant for Au NEs with different radii, indicating that the critical concentration of dissolved H_2 for bubble nucleation/formation at the NE is not related to electrode size [37].

3.7. Formation of single nanobubbles on WS_2@Au NEs

To obtain WS_2 QDs coated Au NEs (WS_2@Au NEs), we soaked the Au NE with a radius of 9 nm into WS_2 QDs solution (2 $mg \cdot mL^{-1}$) for 1 h. Then, WS_2 QDs would be attached on the surface of Au NE through Au−S bonds to obtain the WS_2@Au NE [23]. In order to prove that the WS_2 QDs were successfully self-assembled onto the Au NE surface, we conducted EIS tests on the Au NE and WS_2@Au NE, respectively, and the results are shown in Fig. S6. The charge transfer resistance (R_{ct}) of Au NE (black curve) is 445 Ω. After self-assembly of

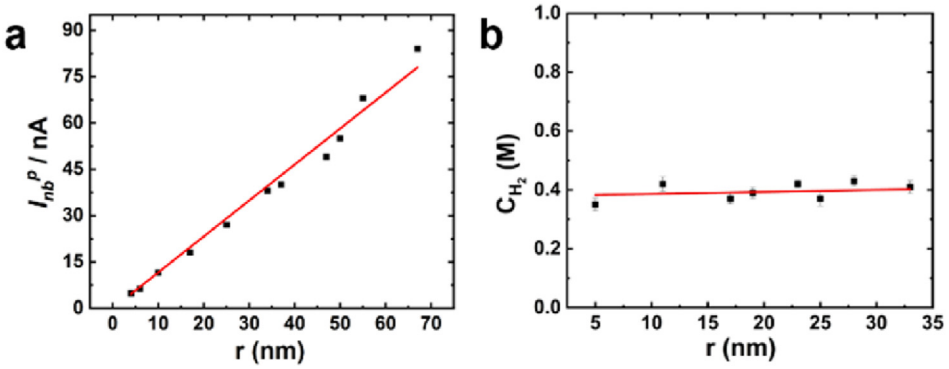

Fig. 3. (a) H_2 nanobubble peak current i_{nb}^{P} as a function of NE radius for H_2 bubble nucleation in 0.5 mol·L^{-1} H_2SO_4. (b) The concentration of dissolved H_2 at the NE surface that is required for bubble nucleation and formation, $C^{s}_{H_2,critical}$, as a function of NE radius. The linear data-fitted lines are included.

WS_2 QDs onto the Au NE surface, the R_{ct} value of WS_2@Au NE increased significantly (578 Ω, red curve). This result proved that the WS_2 QDs were successfully assembled onto the Au NE surface. In order to explore the optimal conditions for generating H_2 bubbles, we optimized the incubation time for the self-assembly of WS_2 QDs onto the Au NE surface. Cyclic voltammetric tests were performed on Au NEs soaked in WS_2 QDs for different time, and the test results are shown in Fig. S7. We found that as the soaking time increases (from 0 to 60 min), the potential corresponding to i_{nb}^{P} moves positively, while at 60 and 80 min of soaking, the potential appears moving negative slightly. According to the different soaking time of Au NE and the corresponding potentials of i_{nb}^{P}, we drew a broken line (Fig. S8a). We found that a soaking time of 60 min produced a potential correction of H_2, so 60 min were selected as the optimal soaking time, and used for all the subsequent related experiments. Fig. S8b compares typical voltammetric responses of Au NE and WS_2@Au NE in H_2SO_4 solution, and the nanobubble formation potential of WS_2@Au NE (−0.522 V) is corrected relative to that of Au NE (−0.8 V), indicating the enhanced HER activity with the modification of WS_2, and further proving the successful modification of WS_2 QDs [36]. However, when the WS_2 QDs are assembled on the Au NE, the larger peak current is required to form H_2 bubbles in the WS_2@Au NE compared to the Au NE, which may be due to the increased surface area [38].

3.8. Microdynamic analysis

We performed microkinetic analysis of the HER processes of Au NEs and Au@WS_2 NEs to evaluate the HER activity. The HER process generally consists of two possible steps, the Volmer step (Eq. 3) and the Heyrovsky or Tafel step (Eq. 4 and Eq. 5), as shown below [37,39,40].

$$\text{Volmer step}: H^+ + e^- + M \rightleftharpoons M - H \quad (3)$$

$$\text{Heyrovsky step}: H^+ + e^- + M - H \rightleftharpoons M + H_2 \quad (4)$$

$$\text{Tafel step}: 2M - H \rightleftharpoons 2M + H_2 \quad (5)$$

where M denotes the surface empty site. The overall rate can be determined by each step, and their corresponding kinetic current expressions can be expressed as [41].

$$i_{et} = nFAk^0 a_{H^+} \exp(-\alpha f\eta) \quad (6)$$

$$i_{et} = nFA\frac{k^0 K^0 a_{H^+}^2 \exp(-\alpha f\eta)}{\exp(f\eta) + K^0 a_{H^+}} \quad (7)$$

$$i_{et} = nFAk^0\left[\frac{K^0 a_{H^+}^2}{\exp(f\eta) + K^0 a_{H^+}}\right]^2 \quad (8)$$

where i_{et} and F are the current flowing under the kinetic limit and the Faraday constant, respectively, and A and k^0 are the electrode surface area and the standard rate constant of the HER rate-determining step, respectively. K^0 and a_{H^+} are the equilibrium constant and proton activity of the Volmer step, respectively. f is equal to F/RT and η is the overpotential, and α is the conversion coefficient of the rate-determining step.

Before data fitting, i_{et} could be obtained by subtracting the contribution of mass transfer from the Koutecký−Levich equation (Eq. 9) [37,42].

$$\frac{1}{i_{et}} = \frac{1}{i} - \frac{1}{i_{mt}} = \frac{1}{i} - \frac{1}{4FD_{H^+}C_{H^+}r} \quad (9)$$

Where i represents the experimentally measured overall current, i_{mt} and D_{H^+} are the limiting current controlled solely by mass transfer of H^+ and diffusion coefficient of H^+ (7.8×10^{-5} cm^2·s^{-1}), respectively. r is the radius of the NE. By fitting the experimental data using the

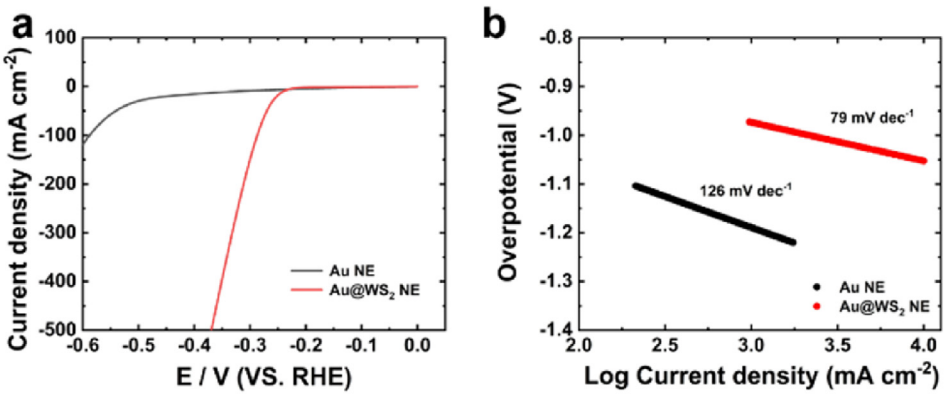

Fig. 4. (a) Polarization curves and (b) the corresponding Tafel plots of Au NE and Au@WS_2 NE (both with 30 nm radius) in a 0.5 mol·L^{-1} H_2SO_4 solution.

three rate-determining formulas provided above, and the correct kinetic model by finding the best result between fit and experiment can be obtained.

After the nonlinear fitting of Eqs. 6–8, the best fit was obtained using Eq. 6 for the Au NE (Fig. S9a), which suggests that the rate-determining step should be the Volmer step in the HER process of Au NE. On the other hand, the Heyrovsky step is the rate-determining step in the HER process of Au@WS_2 NE (Fig. S9b). As reported previously, the Volmer step on the Pt surface is very fast [43], and the rate-determining step of our fitted Au NEs may contradict this. Therefore, in order to further verify the accuracy of the simulation results, the polarization curves and Tafel slopes of Au NE and Au@WS_2 NE with a radius of 30 nm were obtained, as shown in Fig. 4. Tafel slope is used to distinguish different mechanistic pathways in HER. Generally, there are three main reaction steps for HER in acidic electrolytes, including an initial discharge step (Volmer step, Tafel slope of ~120 mV·dec^{-1}), followed by an electrochemical desorption step (Heyrovsky reaction, Tafel slope of ~40 mV·dec^{-1}) or the recombination step where hydrogen is adsorbed on the catalyst surface (Tafel reaction, Tafel slope ~ 30 mV·dec^{-1}). For the HER process, the H_2 generation mechanism step is either a combination of Volmer-Tafel steps or a combination of Volmer-Heyrovsky steps. In Fig. 4b, the Tafel slopes of Au NE and Au@WS_2 NE are 126 mV·dec^{-1} and 79 mV·dec^{-1}, respectively, which are in agreement with the theoretical values, indicating that during HER, the Volmer-Heyrovsky process exists on the Au NE and Au@WS_2 NE. Based on the consistency between experimental results and simulation results, the surface coverage of adsorbed H on the Au@WS_2 NE can be calculated by Eq. 10:

$$\theta = \frac{K^0 a_{H^+}}{\exp(f\eta) + K^0 a_{H^+}} \tag{10}$$

The values of α, k^0, K^0 and θ for the Au NEs and Au@WS_2 NEs are shown in Table S1 and Table S2. At the bubble formation potential, the value of θ is about 0.98, indicating that the adsorbed H protons almost completely cover the Au@WS_2 NEs when the bubbles are formed. In addition, the average k^0 of Au@WS_2 NEs is approximately 12 times that of Au NEs, indicating that Au@WS_2 NEs have higher HER activity. Compared with α, K^0 and θ, k^0 of different NEs showed larger changes, indicating the activity heterogeneity of NEs. This heterogeneity may not only be due to size effects but also result from the structural dispersion observed at the nanoscale [44–47].

4. Conclusions

We have studied the behaviors of single hydrogen bubbles formed on Au NEs and Au@WS_2 NEs based on voltammetry, providing help for understanding the basic research on nanobubble electrochemistry and the evaluation of HER activity. Microkinetic analysis of the voltammetric response showed that the average k^0 of Au@WS_2 NEs was approximately 12 times that of Au NEs, indicating that Au@WS_2 NEs had higher HER activity. As the HER activity increased, the bubble formation potential shifted to a more positive potential. This work can help us design and screen new nanomaterials for the application in fundamental electrochemistry, electrocatalysis and energy-related field, especially at a single entity level.

Supporting information

Additional information as noted in the text. This material is available free of charge via the internet at https://jelectrochem.xmu.edu.cn/journal/.

HER kinetic parameters of Au NEs; HER kinetic parameters of Au@WS_2 NEs; Characterization of a single Au NE; Characterization of WS_2 QDs; XPS spectrum of WS_2 QDs; XRD patterns of WS_2 QDs; CVs of the Au NE with different radius; EIS characterization of Au NE and Au@WS_2 NE; CVs for Au NE in WS_2 QDs after various immersion times; The relationship between Au@WS_2 NEs different soaking time and the voltage of bubble generation; and experimental CVs and their corresponding best fits.

Acknowledgements

We are grateful for financial support from the National Natural Science Foundation of China (No. 21775003), Anhui Provincial Natural Science Foundation (No. 2308085MB56), and the Key Project of Anhui Provincial Department of Education Scientific Research Project (No. 2023AH040032).

Conflict of interest

The authors declare no competing interest.

References

[1] Khaselev O, Turner J A. A monolithic photovoltaic-photoelectrochemical device for hydrogen production via water splitting[J]. Science, 1998, 280(5362): 425−427.
[2] Wang X, Maeda K, Thomas A, Takanabe K, Xin G, Carlsson J M, et al. A metal-free polymeric photocatalyst for hydrogen production from water under visible light[J]. Nat. Mater., 2009, 8(1): 76−80.
[3] Liang Y Y, Li Y G, Wang H L, Zhou J G, Wang J, Regier T, et al. Co_3O_4 nanocrystals on graphene as a synergistic catalyst for oxygen reduction reaction[J]. Nat. Mater., 2011, 10(10): 780−786.
[4] Cheng Y, Xu C, Jia L, Gale J D, Zhang L, Liu C, et al. Pristine carbon nanotubes as non-metal electrocatalysts for oxygen evolution reaction of water splitting[J]. Appl. Catal. B-Environ., 2015, 163: 96−104.
[5] Rees N V, Compton R G. Carbon-free energy: a review of ammonia-and hydrazine-based electrochemical fuel cells [J]. Energy Environ. Sci., 2011, 4(4): 1255−1260.
[6] Meng Y Y, Zou X X, Huang X X, Goswami A, Liu Z W, Asefa T. Polypyrrole-derived nitrogen and oxygen co-doped mesoporous carbons as efficient metal-free electrocatalyst for hydrazine oxidation[J]. Adv. Mater., 2014, 26(37): 6510−6516.
[7] Van Der Linde P, Peñas-López P, Soto Á M, Van Der Meer D, Lohse D, Gardeniers H, et al. Gas bubble evolution on microstructured silicon substrates[J]. Energy Environ. Sci., 2018, 11(12): 3452−3462.
[8] Zhao X, Ren H, Luo L. Gas bubbles in electrochemical gas evolution reactions[J]. Langmuir, 2019, 35(16): 5392−5408.
[9] Angulo A, van der Linde P, Gardeniers H, Modestino M, Rivas D F. Influence of bubbles on the energy conversion efficiency of electrochemical reactors[J]. Joule, 2020, 4(3): 555−579.
[10] Graziano G. Forever blowing nanobubbles[J]. Nat. Rev. Chem., 2020, 4(10). 506−506.
[11] Liu Y L, Jin C, Liu Y W, Chen Q J. Recent progress in gas nanobubble electrochemistry[J]. Sci. China Chem., 2021, 51(3): 310−322.
[12] Luo L, White H S. Electrogeneration of single nanobubbles at sub-50-nm-radius platinum nanodisk electrodes[J]. Langmuir, 2013, 29(35): 11169−11175.
[13] Chen Q, Luo L, Faraji H, Feldberg S W, White H S. Electrochemical measurements of single H_2 nanobubble nucleation and stability at Pt nanoelectrodes[J]. J. Phys. Chem. Lett., 2014, 5(20): 3539−3544.
[14] Chen Q, Luo L, White H S. Electrochemical generation of a hydrogen bubble at a recessed platinum nanopore electrode[J]. Langmuir, 2015, 31(15): 4573−4581.
[15] Chen Q, Wiedenroth H S, German S R, White H S. Electrochemical nucleation of stable N_2 nanobubbles at Pt nanoelectrodes[J]. J. Am. Chem. Soc., 2015, 137(37): 12064−12069.
[16] German S R, Edwards M A, Chen Q, Liu Y, Luo L, White H S. Electrochemistry of single nanobubbles. Estimating the critical size of bubble-forming nuclei for gas-evolving electrode reactions[J]. Faraday Discuss., 2016, 193: 223−240.
[17] Ren H, German S R, Edwards M A, Chen Q, White H S. Electrochemical generation of individual O_2 nanobubbles via H_2O_2 oxidation[J]. J. Phys. Chem. Lett., 2017, 8(11): 2450−2454.
[18] Ren H, Edwards M A, Wang Y, White H S. Electrochemically controlled nucleation of single CO_2 nanobubbles via formate oxidation at Pt nanoelectrodes[J]. J. Phys. Chem. Lett., 2020, 11(4): 1291−1296.
[19] Qiu X, Wei H F, Li R J, Li Y X. Electrochemical and electrocatalytic performance of single Au@ Pt/Au bimetallic nanoparticles[J]. J. Alloy. Compd., 2023, 956: 170365.
[20] Chen W, Wang H, Tang H R, Yang C, Li Y X. Unique voltammetry of silver nanoparticles: from single particle to aggregates[J]. Anal. Chem., 2019, 91(22): 14188−14191.
[21] Duan X H, Li N, Wang G N, Su X G. High sensitive ratiometric fluorescence analysis of trypsin and dithiothreitol based on WS_2 QDs[J]. Talanta, 2020, 219: 121171.
[22] Guo X R, Wang Y, Wu F Y, Ni Y N, Kokot S. The use of tungsten disulfide dots as highly selective, fluorescent probes for analysis of nitrofurazone[J]. Talanta, 2015, 144: 1036−1043.
[23] Pakiari A, Jamshidi Z. Nature and strength of M− S Bonds (M= Au, Ag, and Cu) in binary alloy gold clusters[J]. J. Phys. Chem. A, 2010, 114(34): 9212−9221.
[24] Hua H M, Liu Y, Wang D M, Li Y X. Size-dependent voltammetry at single silver nanoelectrodes[J]. Anal. Chem., 2018, 90(16): 9677−9681.
[25] Li Y X, Wu Q Q, Jiao S F, Xu C D, Wang L. Single Pt nanowire electrode: preparation, electrochemistry, and electrocatalysis[J]. Anal. Chem., 2013, 85(8): 4135−4140.
[26] Watkins J J, Chen J, White H S, Abruna H D, Maisonhaute E, Amatore C. Zeptomole voltammetric detection and electron-transfer rate measurements using platinum electrodes of nanometer dimensions[J]. Anal. Chem., 2003, 75(16): 3962−3971.
[27] Cheng Z L, Ma L, Liu Z. Hydrothermal-assisted grinding route for WS_2 quantum dots (QDs) from nanosheets with preferable tribological performance[J]. Chin. Chem. Lett., 2021, 32(1): 583−586.
[28] Yan Z L, Fu L J, Yang H M, Ouyang J. Amino-functionalized hierarchical porous SiO_2-AlOOH composite nanosheets with enhanced adsorption performance[J]. J. Hazard. Mater., 2018, 344: 1090−1100.
[29] Bayat A, Saievar-Iranizad E. Synthesis of blue photoluminescent WS_2 quantum dots via ultrasonic cavitation[J]. J. Lumines., 2017, 185: 236−240.
[30] Yan Y H, Zhang C L, Gu W, Ding C P, Li X C, Xian Y Z. Facile synthesis of water-soluble WS_2 quantum dots for turn-on fluorescent measurement of lipoic acid[J]. J. Phys. Chem. C, 2016, 120(22): 12170−12177.

[31] Lin L X, Xu Y X, Zhang S W, Ross I M, Ong A CM, Allwood D A. Fabrication of luminescent monolayered tungsten dichalcogenides quantum dots with giant spin-valley coupling[J]. ACS nano, 2013, 7(9): 8214−8223.
[32] Xu S S, Gao X M, Hu M, Sun J Y, Wang D S, Zhou F, et al. Morphology evolution of Ag alloyed WS_2 films and the significantly enhanced mechanical and tribological properties[J]. Surf. Coat. Technol., 2014, 238: 197−206.
[33] Wang Y, Liu Y, Zhang J F, Wu J J, Xu H, Wen X W, et al. Cryo-mediated exfoliation and fracturing of layered materials into 2D quantum dots[J]. Sci. Adv., 2017, 3(12): e1701500.
[34] Shi F Y, Du J R, Han Q, Zhang F R, Wang K, Kan Z T, et al. Integrated wearable foam modified with WS_2 nanosheets@MoS_2 quantum dots for oral disease diagnosis and healthcare monitoring[J]. Chem. Eng. J., 2023, 477: 146800.
[35] Edwards M A, White H S, Ren H. Voltammetric determination of the stochastic formation rate and geometry of individual H_2, N_2, and O_2 bubble nuclei[J]. ACS Nano, 2019, 13(6): 6330−6340.
[36] Chen Q, Ranaweera R, Luo L. Hydrogen bubble formation at hydrogen-insertion electrodes[J]. J. Phys. Chem. C, 2018, 122(27): 15421−15426.
[37] Chen Q J, Luo L. Correlation between gas bubble formation and hydrogen evolution reaction kinetics at nanoelectrodes [J]. Langmuir, 2018, 34(15): 4554−4559.
[38] Wei H F, Wang H, Tang H R, Li Y X. Voltammetric analysis of single nanobubble formation on Ag and Ag@MoS_2 nanoelectrodes[J]. J. Phys. Chem. C, 2021, 125(5): 3073−3080.
[39] Sheng W, Gasteiger H A, Shao-Horn Y. Hydrogen oxidation and evolution reaction kinetics on platinum: acid vs alkaline electrolytes[J]. J. Electrochem. Soc., 2010, 157(11): B1529.
[40] Durst J, Siebel A, Simon C, Hasché F, Herranz J, Gasteiger H A. New insights into the electrochemical hydrogen oxidation and evolution reaction mechanism[J]. Energy Environ. Sci., 2014, 7(7): 2255−2260.
[41] Shinagawa T, Garcia-Esparza A T, Takanabe K. Insight on Tafel slopes from a microkinetic analysis of aqueous electrocatalysis for energy conversion[J]. Sci Rep, 2015, 5(1): 13801.
[42] Hill C M, Kim J, Bard A J. Electrochemistry at a metal nanoparticle on a Tunneling film: a steady-state model of current densities at a tunneling ultramicroelectrode[J]. J. Am. Chem. Soc., 2015, 137(35): 11321−11326.
[43] Defnet P A, Han C, Zhang B. Temporally-resolved ultrafast hydrogen adsorption and evolution on single platinum nanoparticles[J]. Anal. Chem., 2019, 91(6): 4023−4030.
[44] Mariano R G, McKelvey K, White H S, Kanan M W. Selective increase in CO_2 electroreduction activity at grain-boundary surface terminations[J]. Science, 2017, 358(6367): 1187−1192.
[45] Liu C M, Lin H W, Huang Y S, Chu Y C, Chen C, Lyu D R, et al. Low-temperature direct copper-to-copper bonding enabled by creep on (111) surfaces of nanotwinned Cu[J]. Sci Rep, 2015, 5(1): 9734.
[46] Aaronson B DB, Chen C H, Li H, Koper M TM, Lai S CS, Unwin P R. Pseudo-single-crystal electrochemistry on polycrystalline electrodes: visualizing activity at grains and grain boundaries on platinum for the Fe^{2+}/Fe^{3+} redox reaction[J]. J. Am. Chem. Soc., 2013, 135(10): 3873−3880.
[47] Chen C H, Meadows K E, Cuharuc A, Lai S CS, Unwin P R. High resolution mapping of oxygen reduction reaction kinetics at polycrystalline platinum electrodes[J]. Phys. Chem. Chem. Phys., 2014, 16(34): 18545−18552.

纳米电极上单纳米气泡的伏安分析和电催化

罗贤准，陈晓虎，李永新*
安徽师范大学化学与材料科学学院，安徽 芜湖 241000

摘要

利用金纳米盘电极的极小尺寸（Au NEs，半径小于 50 nm），研究了在纳米电极表面产生的单个氢纳米气泡，以评价其析氢性能。我们研究了 Au NEs 在不同浓度硫酸中的电化学行为，结果表明 CV 的形状随着硫酸浓度的增加从 S 型波逐渐变为峰型波。根据纳米气泡的形成机理，得出了产生单个纳米气泡的最小硫酸浓度，表明此时氢气在电极表面达到了临界过饱和，产生了单个纳米气泡和电化学峰型响应。并通过微动力学模型评价了金纳米电极和金@二硫化钨量子点纳米电极（Au@WS_2 NEs）的析氢反应（HER）活性。结果表明，在 Au NEs 表面的临界溶解氢气浓度约为 0.4 mol·L^{-1}，相当于室温和大气压下溶于水中氢气过饱和度的 500 倍。此外，通过对单个纳米气泡形成前的电流强度的微动力学分析，发现 Au@WS_2 NEs 和 Au NEs 析氢反应的决速步骤分别为 Heyrovsky step 和 Volmer step，Au@WS_2 NEs 决速步的标准速率常数（k^0）约为 Au NEs 的 12 倍，表明 Au@WS_2 NEs 具有更高的 HER 活性。随着 HER 活性的增加，气泡形成电位转向更正的电位。这项工作利用极小尺寸的纳米电极甚至包括分子尺寸的纳米电极对其表面产生的单个氢纳米气泡进行研究，为纳米气泡电化学研究提供了基础，并为后续基于气泡的应用提供了新的思路，可以帮助我们设计和筛选应用于基础电化学、电催化和能源相关领域的新型纳米材料，特别是在单个实体水平上。

关键字：纳米电极；纳米气泡；电催化